EarthArXiv Coversheet

Authors

Andrew Gunn[1,♣], Giampietro Casasanta[2], Luca Di Liberto[2], Federico Falcini[3], Nicholas Lancaster[4] & Douglas J. Jerolmack[1,5,♠]

Affiliations

[1]Department of Earth and Environmental Sciences, University of Pennsylvania, Philadelphia, USA
[2]Institute of Atmospheric Sciences and Climate - National Research Council of Italy (CNR-ISAC), Rome, Italy
[3]Institute of Marine Science - National Research Council of Italy (CNR-ISMAR), Rome, Italy
[4]Earth & Ecosystem Sciences, Desert Research Institute, Reno, USA
[5]Department of Mechanical Engineering and Applied Mechanics, University of Pennsylvania, Philadelphia, USA

Emails

[♣]andle@sas.upenn.edu
[♠]sediment@sas.upenn.edu

Peer-review statement

This manuscript is **not** peer-reviewed.

What sets aeolian dune height?

Andrew Gunn[1], Giampietro Casasanta[2], Luca Di Liberto[2], Federico Falcini[3], Nicholas Lancaster[4], and Douglas J. Jerolmack[1,5,*]

[1]Department of Earth & Environmental Sciences, University of Pennsylvania, Philadelphia, USA
[2]Institute of Atmospheric Sciences and Climate - National Research Council of Italy (CNR-ISAC), Rome, Italy
[3]Institute of Marine Science - National Research Council of Italy (CNR-ISMAR), Rome, Italy
[4]Earth & Ecosystem Sciences, Desert Research Institute, Reno, USA
[5]Department of Mechanical Engineering & Applied Mechanics, University of Pennsylvania, Philadelphia, USA
[*]e-mail: sediment@sas.upenn.edu

ABSTRACT

Wherever a loose bed of sand is subject to sufficiently strong winds, aeolian dunes form at wavelengths and growth rates that are well predicted by linear stability theory[1–3]. As dunes mature and coarsen, however, their growth trajectories become more idiosyncratic; nonlinear effects[1], sediment supply[4], wind variability[5] and geologic constraints[6,7] become increasingly relevant, resulting in complex and history-dependent dune amalgamations. Here we examine a fundamental question: do aeolian dunes stop growing and, if so, what determines their ultimate size? Earth's major sand seas are populated by giant sand dunes, evolved over tens of thousands of years[8,9]. We perform a global analysis of the topography of these giant dunes, and their associated atmospheric forcings and geologic constraints, and we perform numerical experiments to gain insight on temporal evolution of dune growth. We find no evidence of a previously proposed limit to dune size by atmospheric boundary layer height[10]. Rather, our findings indicate that dunes may grow indefinitely in principle; but growth slows with increasing size, and may ultimately be limited by sand supply. We also demonstrate that giant dune size depends on both wind climate and sand supply through their control on dune morphology, revealing a topographic signature of geologic and climatic forcing in Earth's sand seas.

Earth's major sand seas are often populated with giant dunes, up to hundreds of meters in height and kilometers in wavelength. These massive sediment piles, visible from space on our planet and across the Solar System, indicate that conditions for sand transport have persisted for millenia. Unraveling how giant dunes form therefore has implications for understanding atmospheric flows and climatic stability. The initial wavelength and growth rate of aeolian dunes from a flat sand bed are well understood; aerodynamic theory developed for idealized conditions has recently been extended and successfully applied to predict dune formation in nature[2,3,11]. Once dunes grow large enough to perturb the flow nonlinearly, however, size regulation becomes more complicated. Dunes calve and merge through collisions and wake interactions[7]; but the net effect is pattern coarsening through time[10,12,13]. Is there any limit to the size that aeolian dunes can grow, besides time? One elegant hypothesis is that the size of giant dunes is limited by the averaged mixed layer height (MLH), where a stable resonance condition is found between topographic and capping-layer waves[10]. This prediction is appealing because it suggests a general and physical (rather than site specific and geological) control by atmospheric forcing, and that the scale of giant dunes can be used to infer the MLH on other planets[14]. An alternative hypothesis, however, is that dune growth just slows logarithmically with time, as dunes grow larger and their migration rates diminish[12]. As real dune fields evolve over century and longer timescales, additional site-specific boundary conditions have been suggested to exert a control on dune size: sediment supply, geologic constraints, wind variability, and climatic stability. Neither the MLH control, or the logarithmic slowing hypothesis, have been directly tested in nature.

Here we develop a two-pronged approach to examine the growth, and possible saturation, of giant aeolian dunes on Earth. We assemble a global data set of large ($>$ 100 m wavelength) dunes, and their associated (modern) atmospheric conditions, for 38 dune fields that includes: dune field area and age; dune geometry (height, width and wavelength) and morphology (barchanoid, transverse, linear and star); MLH; and sand flux. We find no evidence of the proposed control of MLH on dune wavelength. Data reveal, however, that dune size is controlled in part by variability in wind direction, through its influence on dune morphology. Modern dune fields present only a snapshot of the trajectory of dune evolution. To gain insight into temporal dynamics, and potential controls of sand supply and wind variation, we conduct numerical experiments using the well-regarded cellular dune model ReSCAL[15] under a range of geologically-relevant boundary conditions. These experiments corroborate our field interpretations, and suggest that aeolian dune growth has no hard physical limit. Rather, our findings support the logarithmic slowing hypothesis and suggest that sand supply, and potentially the stability of climatic conditions favorable for aeolian transport, may ultimately limit the maximum size dunes can achieve in a particular dune field.

Observations

Global LANDSAT imagery was used to manually identify and delineate the boundaries of 38 dune fields (Methods M1). We utilized ERA-5 reanalysis data to determine 10-m hourly wind velocity for the 2008–2017 decade on a 32-km^2 horizontal grid[16]. Potential sand flux ($\vec{q}$) was estimated from these data with a linear excess stress model that explicitly incorporates an entrainment threshold[1,17] (Methods M2); it is important to note that this corresponds to the saturated sand flux, and true flux could be less if supply is limited. We utilized SRTM ASTER GDEM V3 topography to determine the average dune geometry — wavelength, x, height, z and width, y — within each 32-km^2 tile[18] (Figs. 1 & ED1; Methods M3); topographic resolution prohibits detection of dunes with $x < 100$ m. Corresponding dune morphology was manually categorized into the canonical types; barchanoid, transverse, linear and star[4,5,17]. Taken together, our analysis produces estimates of modern sand flux, and dune geometry and morphology, for 2,093 32-km^2 tiles on Earth. Where possible, we used published data to estimate dune-field age (Methods M1). Mixed layer height was determined using all available daytime CALIPSO satellite measurements collected from 2006 to 2019 over each dune field (Methods M4). These are always collected in the early afternoon, where the boundary layer is convective and most likely to promote sand transport[19], but there is still a clearly identifiable delineation between the aerosol-laden mixed layer at the free-atmosphere above[20].

We first examine patterns in dune geometry for the global dataset. Although previous studies have documented self-similar scaling of barchan dune geometry[21], those observations did not include other dune geometries or giant dunes. Our compiled data show that dune geometry is not self similar for the largest wavelengths, where very high aspect-ratio dunes are observed (Fig. 2a). Plotting width against wavelength produces distinct clouds of data that correspond to dune morphology; barchanoid and star dunes follow a 1:1 line, while linear dunes are the widest and transverse dunes show intermediate behavior (Fig. 2d). Another distinction is that the highest dunes in the dataset ($z > 100$ m) are disproportionately represented by star dunes, which also appear to only form at large wavelengths[9,22] (generally > 1 km) (Fig. 2a). In contrast, aspect-ratio scaling for barchanoid and transverse dunes generally follows observed patterns for subaqueous dunes[23,24].

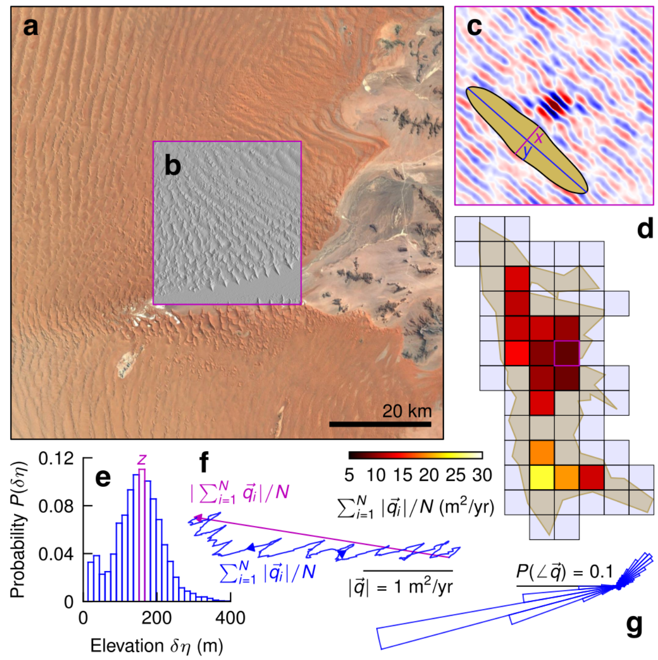

Figure 1. Extraction of dune geometry and sand flux. (**a**) LANDSAT imagery of the Namib Sand Sea, one dune field in the dataset. (**b**) Hillshade SRTM topography from an example 32 km^2 tile. (**c**) The high-pass autocorrelation of the topography in (b) overlaid by the extracted characteristic planform dune geometry in yellow (not to scale, wavelength x in magenta and width y in blue). (**d**) Grid of prospective tiles intersecting the dune field (yellow); tiles included in the dataset (where dune geometry can be measured) are colored by mean sand flux $|\vec{q}|$ inferred from ERA-5 10-m winds. (**e**) Probability distribution of local relief $\delta\eta$ found by convolution of SRTM topography with a min-max box of width x; the peak marks the characteristic dune height z. (**f**) Time-means of the resultant sand flux vector (magenta) and cumulative sand flux vectors (blue) for (b); terms denote their lengths, and arrows their directions. (**g**) The probability distribution of sand flux directions for (b). Black lines denote scale in (a, f & g), N is the number of hourly measurements over the decade of ERA-5 reanalysis, north is up in (a–d, f & g), and magenta boxes in (b–d) outline the common tile.

It is well established that dune morphology is a consequence of variability in wind direction: predominantly unidirectional sand flux results in barchanoid and transverse dunes under conditions of relatively low and high sand supply, respectively; oblique and bi-directional sand flux creates linear dunes; and highly variable sand flux directionality gives rise to star dunes[4,5,17]. How this variability influences dune geometry and ultimate size, however, has not been fully examined. We compute a flux directionality measure that varies from 0 associated with net-zero flux, to 1 corresponding to unidirectional flux[25] (Fig. 1f). Perhaps unexpectedly, ostensibly unidirectional barchanoid and transverse dunes exhibit a wide range of values for flux directionality (Fig. 2b). We attribute this noise to many potential factors, but of high significance are: first, sand flux

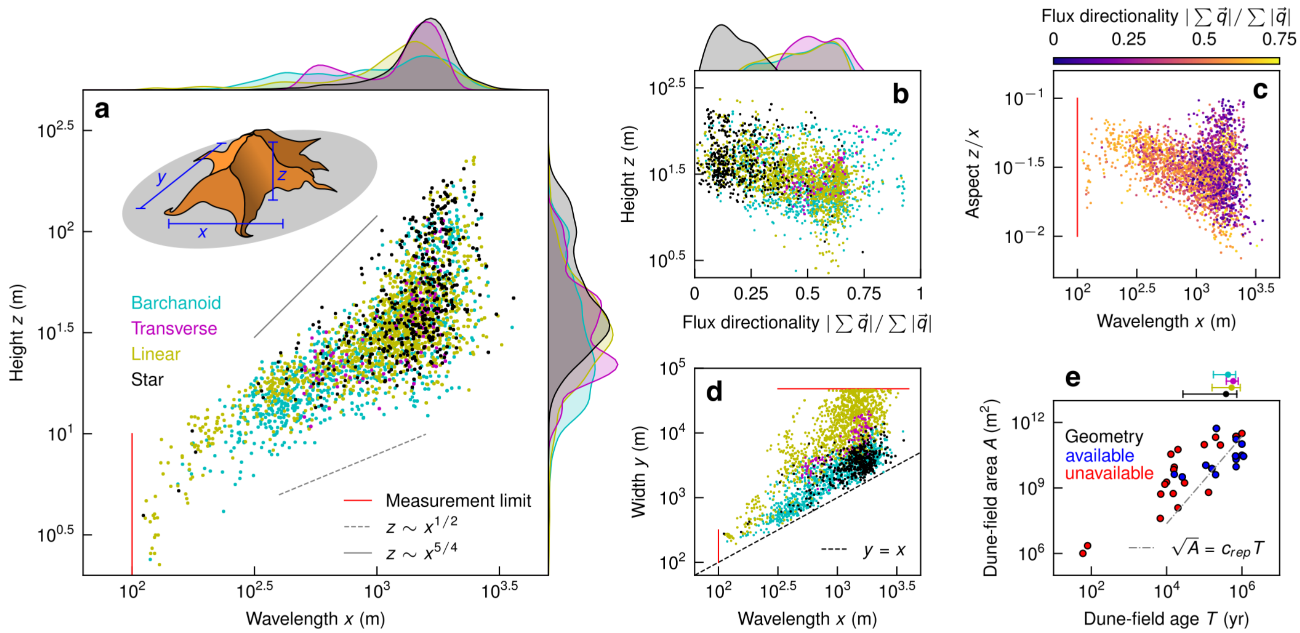

Figure 2. **Trends in Earth's aeolian dunes.** (**a**) Characteristic dune wavelength x and height z for 2,093 32-km^2 tiles. Points and kernel density estimates for each axis colored by type (barchanoid, cyan; transverse, magenta; linear, yellow; star, black), power-laws bounding the distribution given in grey, and a schematic defining x, y and z for an example star dune in upper left. (**b**) Flux directionality (i.e. the resultant sand flux magnitude over the sand flux magnitude sum, or purple over blue in Fig. 1f) against dune height z. Points and kernel density estimate colors defined in (a). (**c**) Dune wavelength x against aspect z/x, points colored by flux directionality using the colorbar above. (**d**) Wavelength x against width y colored as in (a). The dashed black line marks $y = x$, by definition points lie above this line. (**e**) Dune-field age T against area A for 29 dune fields with a powerlaw $\sqrt{A} = c_{rep}T$ (dot-dashed grey line), where c_{rep} (m/yr) is a representative dune migration rate. Blue points ($n = 11$) are included in the geometric analysis, red are not. Using the blue points and sharing the age-axis, dune-type ages (mean $\pm$ standard deviation) are given above the parametric plot. Red lines in (a, c & d) mark measurement limits.

directionality is determined over only 10 years — a relatively short time compared to the age of large dunes in the database — and therefore may not represent formative conditions; and second, sand supply is an important but unmeasured control on sand flux that likely varies significantly across dune fields. Star dunes, however, correspond only to low directionality (high variability) conditions as expected (Fig. 2b). The compiled data also reveal a previously unobserved trend: dune height is inversely related to flux directionality; i.e., dunes with low directionality are relatively taller (Fig. 2b). Indeed, the previously discussed trend of decreasing aspect ratio with increasing wavelength is associated with more undirectional sand-flux regimes, while the cloud of anomalously large aspect ratios corresponds to low directionality (Fig. 2c). These observations suggest that highly variable winds act to "pile up" sand, while more unidirectional winds create lower dunes.

We now turn our attention to the dune-field mixed layer height, and its potential control on the size of giant dunes. Although there are seasonal fluctuations in MLH, and variations among dune fields (Fig. 3), the averaged midday MLH H varies little ($1 < H < 2$ km). Most importantly, we find no correlation between MLH and dune wavelength (Fig. 3b). In other words, data do not support the proposed control of MLH on limiting dune size[10]; in fact, dune wavelength exceeds MLH for most dune fields. To understand why, we must consider the proposed mechanism in light of the atmospheric conditions that give rise to sand transport. The MLH hypothesis assumed that the mixed layer is neutrally stable such that the interface between it and the free-atmosphere at H is a capping interface; in this scenario, large dunes that perturb the flow can excite waves at the interface, which then limit dune wavelength through a resonance condition[10]. While stability conditions that permit this behavior may sometimes occur, our analysis suggests that these conditions are not associated with sand transport. Rather, winds exceeding threshold are typically associated with strong instability[19]; the convection-enhanced mixing that enhances surface wind strength also destroys wave propagation, inhibiting resonance when sand transport occurs (see Text S1 for details).

While our observations are the most comprehensive to date, they still represent only a snapshot in time of the dune coarsening process. Factors important for the evolution of large dunes over millenia, such as sand supply and past variations in wind climate, are completely unconstrained. Further, the central question of what sets aeolian dune height remains unanswered.

To access the trajectory of dune growth through time, and isolate and control boundary conditions that influence dune dynamics, we turn to numerical experiments.

Numerical Experiments

We perform a suite of numerical experiments using ReSCAL[15], a model that couples cellular automaton rules for sediment transport with a lattice gas method for turbulent wind[15]. ReSCAL has been shown to produce many salient aspects of aeolian dune dynamics and morphology[13,15,26], and can be quantitatively scaled to nature[15]. Given that the history and boundary conditions of dune fields examined here are not known, however, we do not attempt a quantitative comparison of model runs with field data. Instead, we perform six numerical experiments that essentially bracket the range of Earth's aeolian landscapes[5]. Model runs conserve sand in a domain that is horizontally periodic. Domain height is set to be sufficiently large that it does not influence dune growth, informed by the lack of MLH control shown previously (Methods M5). The initial conditions are flat sand beds of two thicknesses, $\eta(t=0) = 3.5$ m and $\eta(t=0) = 35$ m, to simulate sediment-starved and sediment-saturated systems, respectively[7]. Three forcing regimes are chosen to mimic winds that produce unidirectional (barchanoid and transverse), linear, and star dune types by varying the number of wind directions F_N; these dune types correspond to flux directionality values of 1, 0.5 and 0, respectively. For $F_N > 1$, directions iterate every 4 months and all experiments are run for over 1,600 years. We verify that the imposed wind forcing produces the expected dune morphologies at the end of the model runs (Fig. 4b).

Each experiment shows that dune height grows approximately logarithmically with time, i.e., $z \sim \log(t)$ (Fig. 4a) as observed in previous dune simulations[12]. Deviations from this behavior are observed for linear dunes, as a result of dislocation repulsion[27]. Systems with high sand supply tend to produce dunes that grow taller (Fig. 4a), following intuition. Unidirectional dunes exhibit sub-linear scaling of height with wavelength indicating a decrease in aspect ratio as dunes grow. Star and linear dunes, by contrast, show super-linear $z-x$ scaling; their height grows more rapidly than unidirectional dunes, and they are relatively taller for all wavelengths (Fig. 4c). These qualitative behaviors are in accord with our observations from natural dune fields (Figs. 2a and 4c). For all conditions, numerical experiments show that dune migration rate (commonly called celerity) slows as dunes grow larger; while this behavior is a well known consequence of mass conservation[13,17,28], higher-order effects like slip-face development and flow shielding may also reduce flux and hence migration rate as dunes become large[12,29]. Notably, star dunes become essentially stationary once their height reaches ≈ 10 m due to their net-zero flux.

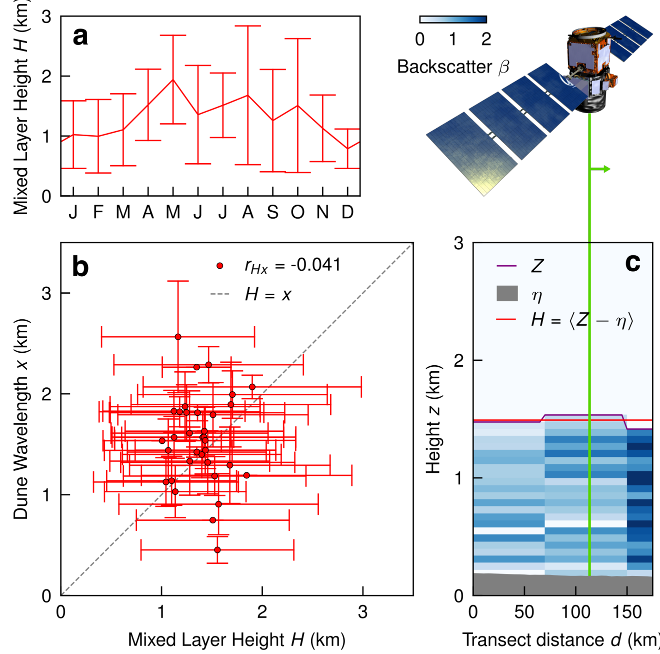

Figure 3. Mixed layer heights over dune fields. (**a**) An example mixed layer height H annual climatology for the Rub Al Khali measured using CALIPSO for 2006-2019. Monthly means and standard deviations given ($n = 222$). (**b**) H and measured dune wavelengths x for 34 dune fields in the geometry data set, means (red dots with black outlines) and standard deviations (red lines) for both measurements are shown, as is the Pearson's correlation coefficient r_{Hx} and the identity $H = x$. If two characteristic dunes are identified in a tile, only the larger one is included in the averaging for this plot. (**c**) An example of the H extraction from CALIPSO (pictured) over the Rub Al Khali. As the satellite passes over the dune field (grey region), the CALIPSO (green line) scan of the atmosphere detects high backscatter β from aerosols in the mixed layer relative to the free atmosphere above (blue map, 5-km horizontal resolution). The elevation η, the mean difference (red line) of the delineation between high and low β, Z, (purple line) and η for the scan constitutes one H value[20].

ReSCAL is subject to uncertainty in the conversion of time and length scales from the virtual to real domain (Methods M6), and the model omits secondary flows in the wind created by topography[15] — which may be particularly important for linear and star dunes[7,22]. Nevertheless, numerical experiments reproduce the main geometric and morphological patterns observed in natural dune fields and laboratory experiments[4,7], giving us some confidence that the temporal dynamics of dune growth in the model have some bearing on natural sand seas. In the absence of MLH control, modeled dunes coarsen indefinitely, but their growth rate slows over time, under constant forcing.

Implications

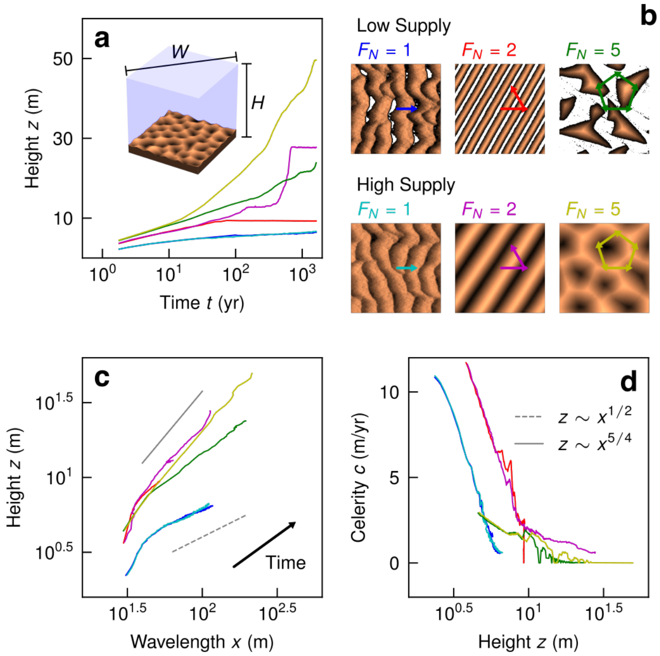

Figure 4. Numerical experiments of dune growth. (**a**) Dune height time-series for ReSCAL experiments. Line colors correspond to experiments shown in (b), a snapshot of the yellow experiment at $t = 162$ yrs shown to define the horizontally-periodic domain; $W = H = 522$ m). (**b**) Planform snapshots of each experiment at the final timestep $t = 1,624$ yrs; color is normalized elevation (dark is lower), white is non-erodible bedrock. The number of flux directions F_N is given, as are the flux vectors for each experiment. The top row of low-supply experiments have $\eta = 3.5$ m of flat sand initially, whereas the bottom row have $\eta = 35$ m of flat sand initially. (**c**) Wavelength x against height z for each experiment coarsening over time; bounding powerlaws from the natural data (legend in (d)) given in Fig. 2a also shown. (**d**) Dune height z against celerity (i.e. migration speed) c.

The distilled interpretation of our findings is this: Earth's giant dunes are growing ever-slower with size, and are not limited in size by MLH or any other hard physical constraint. This calls into question planetary studies that use the capping layer hypothesis to estimate MLH from observed dune wavelength[14]. Nevertheless, the presence of dune fields still places a strong constraint on atmospheric dynamics: near-surface winds must regularly exceed the entrainment threshold, but not by much, in order to maintain saltation that grows dunes[30]. With rudimentary knowledge of the composition of the atmosphere and the sand grains, the dune-forming wind conditions on other planets may be determined with reasonable confidence[31].

Returning to our findings, snapshots of mature dunes in the numerical experiments (taken at $T \gtrsim 500$ yrs) are similar in geometry and morphology to the large dunes populating Earth's surface today. Estimating dune age using available measurements (Methods M1), we see the four morphologies of dunes have similar mean ages; if anything, star dunes are slightly younger than other large dunes (Table ED1, Fig 2e). We conclude that Earth's star and linear dunes, with low flux directionality, are taller because they grow faster; reversing winds act to pile up sand. The numerical experiments also explain other details in the observed data: dune aspect is more sensitive to sediment supply in low flux directionality systems (Figs. 4a & 2c), and ever-slowing coarsening produces the negative skew of dune size probability distributions (Fig. 4a). But these conclusions leave us with a conundrum: why are there no dunes for $x \gtrsim 2$ km, if they always grow? Coarsening rates for such large dunes are exceedingly slow. Over the millenia required to evolve dunes of this size, we hypothesize that climatic and geologic constraints become limiting. First of all, climate must remain sufficiently arid and windy for dunes to remain unvegetated and active; this becomes increasingly unlikely for timescales longer than the Holocene, i.e., 10^4 yr[32,33]. Second of all, sand supply becomes increasingly likely to limit dune growth, as dunes pile sand higher and scour deeper into the substrate; many of the world's giant dunes show signs of sand limitation such as bare non-erodible interdune surfaces[5,22]. While perhaps neither satisfying nor surprising[6,7,34], our findings suggest that both the size and morphology of Earth's largest dunes are the integrated product of the unique geology and climatic history of each dune field. Nevertheless, universal trends in aeolian dune geometry, and the new relations observed between geometry and morphology, may be used to understand where observed dunes sit in their respective growth trajectories.

Our results also contribute to understanding the size of aeolian dune fields themselves[35]. Although scattered, we observe a positive trend in dune-field age (T) against area (A) (Fig. 2e), which could imply that dune-field expansion is driven by dune migration[19,25]. To test this idea, we utilize a representative upper bound on dune migration speeds from the numerical experiments: c_{rep}, the mean celerity after $t > 500$ yr for all six experiments (Fig. 4d). A first-order advective growth scaling can be anticipated, $\sqrt{A} = c_{rep}T$. The data follow the scaling, which indicates that at least some component of dune-field boundary expansion may be driven by dune migration itself. On the other hand, most dune fields lie above the scaling line, indicating they are larger than implied from expansion by dune migration alone; if true, this would suggest that dune-field size is set by sand supply. It seems likely that flux directionality plays some role; in strongly unidirectional cases like White Sands, boundary expansion is clearly related to dune migration[28,36], but for stationary fields of star dunes like the southeast Grand Erg Oriental[22], sand supply must be the dominant factor.

These findings serve as a springboard for investigating how, and how fast, dunes respond to transient forcing. In particular, how will aeolian landscapes adjust to changing climate, and how does their maturity and history influence this change? We see two features of our data that suggest that dunes can be sluggish relative to changing winds. First is the observation of superimposed dunes, with morphologies that are distinct from the larger dunes they ride on[9]. This implies that changing wind may not reorient the entire dune, but rather initiate the formation of new (and much smaller) dunes that slowly cannibalize the underlying larger dune as they grow — as observed for fluvial dunes in response to rapid changes in flow[37,38]. Second is the unexpectedly large variance in flux directionality for ostensibly unidirectional dunes (Fig. 2a), which indicates that many large dunes may have been sculpted by wind conditions that are different from those of the last decade. A rate-and-state framework where dune form, rather than scale, is the measure of landscape adjustment may be useful for understanding dune-field evolution and anticipating dune responses to climate change[39].

References

1. Durán, O., Claudin, P. & Andreotti, B. On aeolian transport: Grain-scale interactions, dynamical mechanisms and scaling laws. *Aeolian Res.* **3**, 243–270 (2011).

2. Gadal, C. *et al.* Spatial and temporal development of incipient dunes. *Geophys. Res. Lett.* **47**, e2020GL088919 (2020).

3. Delorme, P. *et al.* Dune initiation in a bimodal wind regime. *J. Geophys. Res. Earth Surf.* e2020JF005757 (2020).

4. Courrech du Pont, S., Narteau, C. & Gao, X. Two modes for dune orientation. *Geology* **42**, 743–746 (2014).

5. Wasson, R. & Hyde, R. Factors determining desert dune type. *Nature* **304**, 337–339 (1983).

6. Ewing, R. & Kocurek, G. Aeolian dune-field pattern boundary conditions. *Geomorphology* **114**, 175–187 (2010).

7. Pye, K. & Tsoar, H. *Aeolian sand and sand dunes* (Springer Science & Business Media, 2008).

8. Bristow, C. S., Bailey, S. & Lancaster, N. The sedimentary structure of linear sand dunes. *Nature* **406**, 56–59 (2000).

9. Lancaster, N. Controls of eolian dune size and spacing. *Geology* **16**, 972–975 (1988).

10. Andreotti, B., Fourriere, A., Ould-Kaddour, F., Murray, B. & Claudin, P. Giant aeolian dune size determined by the average depth of the atmospheric boundary layer. *Nature* **457**, 1120–1123 (2009).

11. Ping, L., Narteau, C., Dong, Z., Zhang, Z. & Du Pont, S. C. Emergence of oblique dunes in a landscape-scale experiment. *Nat. Geosci.* **7**, 99–103 (2014).

12. Eastwood, E., Nield, J., Baas, A. & Kocurek, G. Modelling controls on aeolian dune-field pattern evolution. *Sedimentology* **58**, 1391–1406 (2011).

13. Gao, X., Narteau, C. & Rozier, O. Development and steady states of transverse dunes: A numerical analysis of dune pattern coarsening and giant dunes. *J. Geophys. Res. Earth Surf.* **120**, 2200–2219 (2015).

14. Lorenz, R. D., Claudin, P., Andreotti, B., Radebaugh, J. & Tokano, T. A 3 km atmospheric boundary layer on titan indicated by dune spacing and huygens data. *Icarus* **205**, 719–721 (2010).

15. Narteau, C., Zhang, D., Rozier, O. & Claudin, P. Setting the length and time scales of a cellular automaton dune model from the analysis of superimposed bed forms. *J. Geophys. Res. Earth Surf.* **114** (2009).

16. Hersbach, H. *et al.* The era5 global reanalysis. *Q. J. Royal Meteorol. Soc.* **146**, 1999–2049 (2020).

17. Bagnold, R. A. *The physics of blown sand and desert dunes* (Courier Corporation, 1941).

18. NASA, M. Aist, japan space systems, and us/japan aster science team. *ASTER Glob. Digit. Elevation Model. V003 [Data set]* (2009).

19. Gunn, A. *et al.* Circadian rhythm of dune-field activity. *Geophys. Res. Lett.* e2020GL090924 (2021).

20. Vaughan, M. A. *et al.* Fully automated analysis of space-based lidar data: An overview of the calipso retrieval algorithms and data products. In *Laser radar techniques for atmospheric sensing*, vol. 5575, 16–30 (International Society for Optics and Photonics, 2004).

21. Elbelrhiti, H., Andreotti, B. & Claudin, P. Barchan dune corridors: field characterization and investigation of control parameters. *J. Geophys. Res. Earth Surf.* **113** (2008).

22. Lancaster, N. Star dunes. *Prog. Phys. Geogr.* **13**, 67–91 (1989).

23. Cisneros, J. *et al.* Dunes in the world's big rivers are characterized by low-angle lee-side slopes and a complex shape. *Nat. Geosci.* **13**, 156–162 (2020).

24. La Forgia, G., Adduce, C., Falcini, F. & Paola, C. Migrating bedforms generated by solitary waves. *Geophys. Res. Lett.* **46**, 4738–4746 (2019).

25. Wilson, I. G. Desert sandflow basins and a model for the development of ergs. *Geogr. J.* 180–199 (1971).

26. Lucas, A. *et al.* Sediment flux from the morphodynamics of elongating linear dunes. *Geology* **43**, 1027–1030 (2015).

27. Werner, B. Eolian dunes: computer simulations and attractor interpretation. *Geology* **23**, 1107–1110 (1995).

28. Jerolmack, D. J. *et al.* Internal boundary layer model for the evolution of desert dune fields. *Nat. Geosci.* **5**, 206–209 (2012).

29. Nield, J. M. & Baas, A. C. The influence of different environmental and climatic conditions on vegetated aeolian dune landscape development and response. *Glob. Planet. Chang.* **64**, 76–92 (2008).

30. Jerolmack, D. J. & Brzinski III, T. A. Equivalence of abrupt grain-size transitions in alluvial rivers and eolian sand seas: A hypothesis. *Geology* **38**, 719–722 (2010).

31. Gunn, A. & Jerolmack, D. J. Conditions for aeolian transport in the solar system. *EarthArXiv* (2020).

32. Vermeesch, P. *et al.* Sand residence times of one million years in the namib sand sea from cosmogenic nuclides. *Nat. Geosci.* **3**, 862–865 (2010).

33. Rodríguez-López, J. P., Clemmensen, L. B., Lancaster, N., Mountney, N. P. & Veiga, G. D. Archean to recent aeolian sand systems and their sedimentary record: current understanding and future prospects. *Sedimentology* **61**, 1487–1534 (2014).

34. Kocurek, G. & Lancaster, N. Aeolian system sediment state: theory and mojave desert kelso dune field example. *Sedimentology* **46**, 505–515 (1999).

35. Kocurek, G. Aeolian system response to external forcing factors—a sequence stratigraphic view of the saharan region. *Quat. Deserts Clim. Chang.* 327–337 (1998).

36. Gunn, A. *et al.* Macroscopic flow disequilibrium over aeolian dune fields. *Geophys. Res. Lett.* **47**, e2020GL088773 (2020).

37. Martin, R. L. & Jerolmack, D. J. Origin of hysteresis in bed form response to unsteady flows. *Water Resour. Res.* **49**, 1314–1333 (2013).

38. Myrow, P. M., Jerolmack, D. J. & Perron, J. T. Bedform disequilibrium. *J. Sedimentary Res.* **88**, 1096–1113 (2018).

39. Lancaster, N. *et al.* Late pleistocene and holocene dune activity and wind regimes in the western sahara desert of mauritania. *Geology* **30**, 991–994 (2002).

Data availability

All SRTM ASTER GDEM v3[18] and CALIPSO[20] data is available on the NASA Earthdata site `https://earthdata.nasa.gov/`. Specific CALIPSO MLH heights used in this study are available in Table S1. ERA-5 reanalysis[16] data are available on the Climate Data Store site `https://cds.climate.copernicus.eu/`. Dune-field age data is drawn from the INQUA Dune Atlas here `https://www.dri.edu/inquadunesatlas/`. All processed dune geometry data is available in Table S2.

Code availability

Code to reproduce this paper can be found at `https://github.com/algunn/giant-dunes`.

Acknowledgements

We thank Michael Kurgansky, Cyril Gadal, Clément Narteau, Olivier Rozier, Philippe Claudin, Orencio Durán & Raleigh Martin for useful discussions.

Author contributions

Formal Analysis, Software, Validation, Visualization and Writing–original draft, A.G.; Conceptualization and Methodology, D.J.J., F.F., A.G.; Data Curation and Investigation, A.G., G.C., N.L.; Project Administration, Writing–review & editing, all authors; Resources, Funding Acquisition, Supervision, D.J.J..

Competing interests

The authors declare no competing interests.

Materials & Correspondence

All correspondence should be directed to Douglas Jerolmack (sediment@sas.upenn.edu).

Methods

M1 Dune-field ages & areas

Dune-field age estimates are found from a literature review[32,M1–M23] and summarized in Table ED2. These data are a subset of the INQUA Dune Atlas[M24]. Methods of estimation are from geochemical and optical dating techniques of the sediments beneath dune fields, aeolian accumulation rates and deposit thicknesses, and aerial imagery. Uncertainty in each age is subject to a variety of inconsistent processes and is reported differently across the data aggregation. Dune-field areas are found simply by tracing the dune-field extent in Google Earth using LANDSAT imagery, also provided in Table ED2.

M2 Sand flux from ERA-5 reanalysis

A time-series of 87,672 hourly 10-m winds $\vec{U_{10}}$ (m/s) from 2008-2017 inclusive are transformed into approximate sand flux $\vec{q}$ (m^2/s) using a standard and consistent approach using threshold friction velocity. Friction velocity, u_*, is calculated as $u_* = |\vec{U_{10}}|\kappa/\log(10/z_0)$, where $\kappa = 0.41$ is von Karman's constant and $z_0 = 10^{-3}$ m is the roughness length at the scale of sand transport[36]. Next a threshold friction velocity is defined as $u_{*,cr} = \sqrt{gd\rho_s/\rho_f}/10$, where $g = 9.81$ m/s^2 is gravity acceleration, $d = 300$ μm is grain diameter, $\rho_s = 2650$ kg/m^3 is sand density and $\rho_f = 1.225$ kg/m^3 is fluid (air) density, giving $u_{*,cr} = 0.252$ m/s as a representative value[17]. Finally sand flux magnitude is defined as $\vec{q} = \{\angle\vec{U_{10}}, 25\rho_f/\rho_s\sqrt{d/g}(u_*^2 - u_{*,cr}^2)\}$ for $u_* > u_{*,cr}$ and $\vec{q} = \{\mathrm{NaN}, 0\}$ otherwise[1]. In lieu of grain-size data for all locations, we chose constants for this calculation that are representative for Earth and not specific to any particular dune field.

M3 Dune geometry extraction

Planform dune geometry is found through the following process. First, an auto-correlation R_η of a 32-km^2 tile of ASTER topography $\eta(\lambda,\phi)$ (where λ is longitude and ϕ is latitude) is created using FFT. The two largest modes are omitted so that any broad, non-dune slopes in the topography do not impact dune-pattern identification; and the square tile is masked by a circle so that dune width is not biased by orientation. We take specific level-sets $\partial\Omega_\alpha = \{(R_\lambda, R_\phi)|R_\eta = \alpha, \Omega_\alpha \ni (0,0)\}$ for $0 < \alpha < \max\{R_\eta\}$ of $R_\eta(R_\lambda, R_\phi)$ that bound the origin as shapes which represent the planform dune geometry. Taking $\partial\Omega_0$ is a poor level-set since patterns are complex and include dislocations. Instead, we identify the appropriate level-sets by finding one or two local maxima in a plot of α against $\chi = A(\Omega_\alpha)/A(\mathrm{conv}(\Omega_\alpha))$, the ratio of level-set area $A(\Omega_\alpha) = \int\int \Omega_\alpha dR_\lambda dR_\phi$ over its convex hull area $A(\mathrm{conv}(\Omega_\alpha)) = \int\int \mathrm{conv}(\Omega_\alpha) dR_\lambda dR_\phi$. We take the only, or two largest $A(\Omega_\alpha)$, maxima, excluding trivial maxima where $A(\Omega_\alpha) > (1-\varepsilon)A(\mathrm{conv}(\Omega_\alpha))$ or $A(\Omega_\alpha) \ll A(\mathrm{conv}(\Omega_\alpha))$, as the planform shape of dunes in the tile. This is unless there is no local maxima because $\chi(\alpha)$ decays monotonically, in which case we found $\chi(\alpha) = 1.1$ as the representative level-set. Overall this method is robust and general for all tiles and allows extraction of the sole dune type, or both dune types if one is superimposed on the other, in the tile. The level-set is then converted from longitude-latitude coordinates to local meters and finally dune wavelength x_{auto} and width y_{auto} are defined as its short- and long-axes, respectively.

Dune height is then extracted afterward by first convolving a min-max box of width x_{auto} (in lon-lat) across $\eta(\lambda,\phi)$, which gives a map $\delta\eta(\lambda,\phi)$ where each point has the value of the local range in η within $x_{auto}/2$ in λ or ϕ. The peak of a histogram of this elevation range map $\delta\eta$ is defined as the characteristic dune height z_{auto}.

After automatic calculation of all tiles, planform and vertical dimensions were then calibrated against a random subset ($n = 25$) of manually extracted geometries using ImageJ with a linear scaling such that $x/x_{auto} = y/y_{auto} = 1.51$ and $z/z_{auto} = 0.85$. This method is outlined in Figure ED1 and processed geometry data are available in Table S2.

M4 Mixed layer height measurements

MLH values are found from the CALIPSO version V4-20 Level 2 aerosol layer product[20]. We identify the MLH as the lowest reported aerosol layer top height extracted from the backscatter profile at 5-km horizontal spacing over circular regions of interest (ROI) centered on each dune field. This method has been extensively evaluated in multiple cases[M25–M27]. The ROIs for each dune field have different diameters as to reflect the dune-field size and avoid any domains adjacent to the dune fields that have significantly different MLH dynamics. Four dune fields (Namib Sand Sea, Sinai Negev Erg, Wahiba Sands and Gran Desierto) were omitted from the CALIPSO data collection because they are coastal, where MLH dynamics are most strongly influenced by the ocean. All daytime profiles (since CALIOP is sun-synchronous) from instrument inception to the end of 2019 were collected within each ROI resulting in $n = 5,784$ MLH values. Profiles were collected for 34 dune fields such that there was no significant bias in observation times toward certain seasons for any dune field. MLH values and ROI radii are given in Table S1 and a comparison to the Andreotti *et al.*[10] implicit measurement is given in Figure ED2.

M5 Numerical experiment set-up & analysis

ReSCAL[15,M28], an open-source parallelizable code, is used to simulate dune growth. Details on the cellular automaton (CA) and lattice gas rules are published elsewhere extensively, notably by Narteau *et al.*[15]. Relative occurrence of CA transition rules that develop topography through fluid transport and avalanches are set by rate Λ and threshold stress τ constants. We use the following values and note dune morphology and dynamics are generally insensitive to $O(1)$ changes in these parameters[M29]: $\{\Lambda_E, \Lambda_C, \Lambda_D, \Lambda_G, \Lambda_T, \tau_1, \tau_2\} = \{4/t_0, 2/t_0, 0.02/t_0, 10^3/t_0, 3/t_0, 200\tau_0, 1000\tau_0\}$, for subscripts erosion (E), deposition (C), diffusion (D), gravity (G), transport (T), initiation (1) and saturation (2), respectively, where τ_0 is the simulation stress scale.

The experiment domains are as follows. The fluid box is $750l_0$ wide and $750l_0 + \eta_0$ tall for all experiments, where l_0 is the grid spacing and η_0 is the initial sediment bed thickness. The sediment domain for $F_N = 1$ simulations is $750l_0$ wide and for $F_N > 1$ experiments, the sediment domain is $530l_0 \approx 750\sqrt{2}l_0$ wide so that the square sediment base can be rotated within the flow to simulate changing wind directions. The sediment domain is horizontally periodic such that sediment is conserved and is initialized as a flat bed of $\eta_0 = \{5l_0, 50l_0\}$ depending on the experiment. The fluid box is periodic in that the forcing is constant everywhere and is in equilibrium with the topography (reached offline from initialization for every change in direction before being allowed to interact with the topography). For $F_N > 1$ experiments the fluid flow direction is changed (that is, the sediment bed is rotated within the unidirectional fluid domain) at $200t_0$ intervals, where t_0 is the time step. All experiments are run for 10^4 timesteps. Movie S1 shows planform views of the experiments.

Dune geometry is found in the experiments in the following way, simplified from Methods M3 since the simulated topography is better behaved. Wavelength x_{auto} is defined as double the closest distance from the origin of the autocorrelation R_η of the elevation η to where $R_\eta = 0$. Height z is $\langle \delta\eta \rangle + \sigma_{\delta\eta}$ where $\delta\eta = \eta \star X$ as in Methods M3. The convolution box X gives the local $\max\{\eta\} - \min\{\eta\}$ within width x_{auto}. Wavelength x is then calibrated against manual measurement such that $x/x_{auto} = 2.21$. Dune celerity c is found using the distance d from the origin to the peak of a cross-correlation $\eta(t) \star \eta(t + \tau_{lag})$ such that $c = d/\tau_{lag}$. Since dunes slow down over time, τ_{lag} is chosen such that it increases linearly over time from $500t_0$ to $2 \cdot 10^4 t_0$ during the experiment duration to ensure no aliasing or spurious stationarity.

M6 Numerical experiment scaling

The conversion from ReSCAL simulation timesteps t_0 and grid-spacings l_0 to real-world units of years and meters are not set *a priori* but instead must be found by comparing real-world constants to those found through targeted numerical experiments[15,M29]. This is because the scales in the simulation are clearly below the dune-scale and above the grain-scale, and hence they depend on the chosen Λ and τ constants[M29] (Methods M5). We note that the conversion will depend on specific details of observed real-world constants also, and these vary across dune fields; as in Methods M2, we take representative global values for comparison.

To find l_0 we take the approach of Narteau *et al.*[15] where we match the length-scale of incipient real-world dunes λ_r (m) to those in ReSCAL λ_s/l_0 such that $l_0 = \lambda_r/(\lambda_s/l_0)$ (m). The incipient dune wavelength has been shown in the field[2,3] to obey $\lambda_r = 2\pi L_{sat}\mathcal{A}/(\mathcal{B} - (u_{*,cr}/\overline{u_*})^2/\mu)$, where $L_{sat} = 2.2d\rho_s/\rho_f$. Hydrodynamic constants are $\mathcal{A} = 3.6$ & $\mathcal{B} = 1.9$, friction angle is $\mu = \tan(34°)$, from the ERA-5 measurements we find the global mean of the critical to mean above-threshold friction velocity as $u_{*,cr}/\overline{u_*} = 0.809$, and representative values of grain diameter $d = 300$ μm, $\rho_s = 2650$ kg/m^3 and $\rho_f = 1.225$ kg/m^3 are taken. This leaves us with a reasonable incipient dune wavelength of $\lambda_r = 34.7$ m[1–3]. In ReSCAL we measure the dispersion relation $\sigma(k)$ for wavenumbers $k = 2\pi/\lambda$ and find $k_{max} = k|_{\partial\sigma(k)/\partial k = 0}$ as the most unstable mode and $\lambda_s = 2\pi/k_{max}$. This is done by blowing wind over sand strips of small-amplitude perturbations of wavenumbers k and watching the decay or amplification of topography like $\ln(\eta) \sim \sigma t_0$. We find $\lambda_s/l_0 = 49.9$, giving $l_0 = 0.698$ m. See Figure ED3a & c for the dispersion relationship and the experiment to measure it.

To find t_0 we must match sand flux magnitudes in the real-world Q_r (m^2/yr) and ReSCAL $Q_s t_0/l_0^2$. In the real-world we simply find the mean $Q_r = \overline{|\vec{q_r}|} = 12.78$ m^2/yr from the ERA-5 measurements (Methods M2). In the simulations $Q_s = q_{s,sat}$ which can be found from the ratio $q_{s,sat}/q_{s,0,sat} = 0.171$, known for $\tau_1 = 200\tau_0$, and $q_{s,0,sat}t_0/l_0^2$ (15). Then the timestep can be calculated as $t_0 = l_0^2(Q_s t_0/l_0^2)/Q_r$ (yr) using the l_0 calculated previously. To find $q_{s,0,sat}t_0/l_0^2$, we measure sand flux downwind of a non-erodible to erodible bed transition with $\tau_1 = 0\tau_0$ and all other parameters as in the numerical experiments[15]. The flux increases from the transition and saturates like $q/q_{sat} = (1 - e^{-D/L_{sat}})$ where D is distance downwind of the transition[M29]. We find that $q_{s,0,sat}t_0/l_0^2 = 0.25$, making $t_0 = 14.2$ hours. See Figure ED3b & d for the $q_{s,0,sat}$ calculation and the experiment to measure it.

References

[M1] Muhs, D. R. *et al.* Origin of the sinai–negev erg, egypt and israel: mineralogical and geochemical evidence for the importance of the nile and sea level history. *Quat. Sci. Rev.* **69**, 28–48 (2013).

[M2] Farrant, A. R. *et al.* Developing a framework of quaternary dune accumulation in the northern rub'al-khali, arabia. *Quat. Int.* **382**, 132–144 (2015).

[M3] Radies, D., Preusser, F., Matter, A. & Mange, M. Eustatic and climatic controls on the development of the wahiba sand sea, sultanate of oman. *Sedimentology* **51**, 1359–1385 (2004).

[M4] Singhvi, A. *et al.* A 200 ka record of climatic change and dune activity in the thar desert, india. *Quat. Sci. Rev.* **29**, 3095–3105 (2010).

[M5] Liu, W. *et al.* Onset of permanent taklimakan desert linked to the mid-pleistocene transition. *Geology* (2020).

[M6] Wang, F. *et al.* Formation and evolution of the badain jaran desert, north china, as revealed by a drill core from the desert centre and by geological survey. *Palaeogeogr. Palaeoclimatol. Palaeoecol.* **426**, 139–158 (2015).

[M7] Li, Z. *et al.* Chronology and paleoenvironmental records of a drill core in the central tengger desert of china. *Quat. Sci. Rev.* **85**, 85–98 (2014).

[M8] Yang, X. *et al.* Initial insights into the age and origin of the kubuqi sand sea of northern china. *Geomorphology* **259**, 30–39 (2016).

[M9] Hesse, P. P. How do longitudinal dunes respond to climate forcing? insights from 25 years of luminescence dating of the australian desert dunefields. *Quat. Int.* **410**, 11–29 (2016).

[M10] Beveridge, C. *et al.* Development of spatially diverse and complex dune-field patterns: Gran desierto dune field, sonora, mexico. *Sedimentology* **53**, 1391–1409 (2006).

[M11] Lancaster, N. & McCarley-Holder, G. Decadal-scale evolution of a small dune field: Keeler dunes, california 1944–2010. *Geomorphology* **180**, 281–291 (2013).

[M12] Bogle, R., Redsteer, M. H. & Vogel, J. Field measurement and analysis of climatic factors affecting dune mobility near grand falls on the navajo nation, southwestern united states. *Geomorphology* **228**, 41–51 (2015).

[M13] Kocurek, G. *et al.* White sands dune field, new mexico: age, dune dynamics and recent accumulations. *Sedimentary Geol.* **197**, 313–331 (2007).

[M14] Derickson, D., Kocurek, G., Ewing, R. C. & Bristow, C. Origin of a complex and spatially diverse dune-field pattern, algodones, southeastern california. *Geomorphology* **99**, 186–204 (2008).

[M15] Sweeney, M. R., McDonald, E. V., Chabela, L. P. & Hanson, P. R. The role of eolian-fluvial interactions and dune dams in landscape change, late pleistocene- holocene, mojave desert, usa. *Geol. Soc. Am. Bull.* (2020).

[M16] Madole, R. F., Mahan, S. A., Romig, J. H. & Havens, J. C. Constraints on the age of the great sand dunes, colorado, from subsurface stratigraphy and osl dates. *Quat. Res.* **80**, 435–446 (2013).

[M17] Yang, X. *et al.* Initiation and variation of the dune fields in semi-arid china–with a special reference to the hunshandake sandy land, inner mongolia. *Quat. Sci. Rev.* **78**, 369–380 (2013).

[M18] Liang, X. Warming-induced eolian accumulation of a chinese high latitude dune field during the last deglaciation. *IN REVIEW* .

[M19] Halfen, A. F., Fredlund, G. G. & Mahan, S. A. Holocene stratigraphy and chronology of the casper dune field, casper, wyoming, usa. *The Holocene* **20**, 773–783 (2010).

[M20] Stokes, S. & Gaylord, D. R. Optical dating of holocene dune sands in the ferris dune field, wyoming. *Quat. Res.* **39**, 274–281 (1993).

[M21] Mayer, J. H. & Mahan, S. A. Late quaternary stratigraphy and geochronology of the western killpecker dunes, wyoming, usa. *Quat. Res.* **61**, 72–84 (2004).

[M22] Gaylord, D. R., Foit Jr, F. F., Schatz, J. K. & Coleman, A. J. Smith canyon dune field, washington, usa: relation to glacial outburst floods, the mazama eruption, and holocene paleoclimate. *J. arid environments* **47**, 403–424 (2001).

[M23] Mason, J. A., Swinehart, J. B. & Loope, D. B. The nebraska sand hills. In *Inland Dunes of North America*, 181–206 (Springer, 2020).

[M24] Lancaster, N. *et al.* The inqua dunes atlas chronologic database. *Quat. Int.* **410**, 3–10 (2016).

[M25] Leventidou, E. *et al.* Factors affecting the comparisons of planetary boundary layer height retrievals from calipso, ecmwf and radiosondes over thessaloniki, greece. *Atmospheric Environ.* **74**, 360–366 (2013).

[M26] Korhonen, K. *et al.* Atmospheric boundary layer top height in south africa: measurements with lidar and radiosonde compared to three atmospheric models. *Atmospheric Chem. Phys.* **14**, 4263–4278 (2014).

[M27] Nakoudi, K., Giannakaki, E., Dandou, A., Tombrou, M. & Komppula, M. Planetary boundary layer height by means of lidar and numerical simulations over new delhi, india. *Atmospheric Meas. Tech.* **12** (2019).

[M28] Rozier, O. & Narteau, C. A real-space cellular automaton laboratory. *Earth Surf. Process. Landforms* **39**, 98–109 (2014).

[M29] Gao, X., Zhang, D., Rozier, O. & Narteau, C. Transport capacity and saturation mechanism in a real-space cellular automaton dune model. *Adv. Geosci.* **37**, 47–55 (2014).

Extended Data

Name	Av. Lon.	Av. Lat.	Area (km^2)	Age (Kyr)	No. tiles	% Barch.	% Trans.	% Linear	% Star
Namib Sand Sea	15.3	-24.9	31,512	1,000[32]	15	5	0	66	27
Grand Erg Occidental	0.7	30.4	72,725	-	64	38	1	42	16
Grand Erg Oriental	7.3	31.0	182,744	-	173	20	0	14	65
West Erg Issaouane	6.7	26.9	4,854	-	1	0	0	0	100
East Erg Issaouane	7.8	27.5	27,579	-	24	34	0	34	31
Idehan Ubari	11.8	27.2	63,209	-	57	30	0	45	23
Idehan Murzuk	13.1	24.9	57,416	-	45	22	0	33	44
Central Grand Sand Sea	25.0	27.4	167,921	-	145	0	0	64	35
Dakhla Farafra	28.7	26.5	8,797	-	3	0	0	100	0
Sinai Negev Erg	33.2	30.7	10,884	110[M1]	3	0	0	0	100
An Nafud & Ad Dahna	43.0	27.6	119,612	-	75	52	0	32	14
Rub Al Khali	50.8	20.6	527,163	210[M2]	470	38	1	47	12
Ramlat Al Sabatayn	46.2	15.5	10,110	-	5	14	0	85	0
Wahiba Sands	58.9	21.9	7,635	160[M3]	5	28	0	71	0
West Registan Desert	63.0	29.6	5,544	-	2	0	0	100	0
Kharan Desert	64.5	28.0	7,884	-	3	50	0	50	0
Karakum Desert	62.1	39.1	2,162	-	1	100	0	0	0
Thar Desert	69.7	26.6	4,012	200[M4]	4	80	0	20	0
Rig-e Jenn	53.7	34.0	4,506	-	1	100	0	0	0
Rig-e Yalan	59.5	30.3	7,069	-	5	0	0	37	62
East Registan Desert	65.5	30.5	15,409	-	10	81	18	0	0
Southwest Takla Makan	79.0	38.2	24,229	700[M5]	23	95	0	4	0
Northwest Takla Makan	80.0	39.3	20,310	700[M5]	19	77	0	22	0
Central Takla Makan	84.0	39.2	168,779	700[M5]	181	62	14	22	0
East Takla Makan	89.0	40.2	9,331	700[M5]	6	100	0	0	0
Kumtag Desert	92.1	39.8	16,683	-	9	0	0	58	41
Badain Jaran Desert	101.8	40.4	28,112	1,100[M6]	33	11	0	44	44
Tengger Desert	104.3	38.5	28,723	680[M7]	12	50	0	43	6
Ulan Buh Desert	106.4	39.9	3,529	-	2	33	0	33	33
Hobp Desert	108.3	40.5	4,172	160[M8]	1	100	0	0	0
Munga-Thirri	136.9	-25.0	101,813	1,000[M9]	86	0	0	100	0
Yamma Yamma	141.3	-26.8	3,949	-	1	0	0	100	0
Gran Desierto	-114.1	31.9	3,169	26[M10]	3	25	0	25	50
Ergs Iguidi & Chech	-2.9	26.7	163,100	-	138	9	0	71	19
Aoukar	-9.3	17.7	44,831	-	35	46	53	0	0
El Djouf	-6.3	19.8	454,564	-	385	49	5	45	0
Azefal, Akchar & Agneitir	-14.6	20.6	32,654	-	9	60	0	40	0
Trarza Reion Desert	-14.4	18.3	44,882	-	39	41	4	54	0
Total (n=38)	-	-	**2,491,596**	-	**2,093** (861)	**34** (38)	**3** (3)	**45** (48)	**15** (9)

Table ED1. Dune fields in geometric analysis. Dune-field centroid coordinates are given in the second and third columns. Ages given for dune fields where measured by the studies referenced. Column 'No. tiles' refers to the number of 32-km^2 tiles where geometry was measured in a given dune field (e.g. the tiles with thicker black outline in Fig 1d). The right-most four columns are the percentage occurrence of barchan, transverse, linear and star dunes, respectively, manually identified for each dune field in its tiles. The right-most four columns in the 'Total' row are average percentages across all tiles, i.e. the global percentage occurrence of each dune type. The non-bold values in brackets in the 'Total' row are for the subset where the dune field age is known.

Name	Area (km^2)	Age (Kyrs)	Technique
Keeler	1	0.06[M11]	RAP
Grand Falls	2.25	0.08[M12]	RAP
White Sands Dune Field	520	7[M13]	OSL
Algodones	1,696	30[M14]	OSL
Kelso Dunes	122	20[M15]	OSL
Gran Desierto*	3,169	26[M10]	OSL
Munga-Thirri*	101,813	1,000[M9]	TL & OSL
Strzlecki	95,643	100[M9]	TL & OSL
Mallee	91,458	268[M9]	TL & OSL
Namib Sand Sea*	312,513	1,000[32]	^{10}Be, ^{26}Al & ^{21}Ne
Sinai Negev Erg*	10,884	110[M1]	OSL
Takla Makan*	226,596	700[M5]	MR
Great Sand Dunes	625	130[M16]	OSL
Badain Jaran Desert*	28,113	1,100[M6]	ESR
Tengger Desert*	28,723	680[M7]	MR
Wahiba Sands*	7,635	160[M3]	IRSL
Hobp Desert*	8,879	16[M8]	OSL
Hushandake	34,928	13[M17]	OSL
Hulunbeir	6,878	15.5[M18]	OSL
Rub Al Khali*	527,163	210[M2]	OSL
Casper	1,821	10[M19]	OSL
Ferris	1,467	9[M20]	OSL
Killpecker	550	15[M21]	OSL
Smith Canyon	40	6.8[M22]	SI
Thar Desert*	208,900	200[M4]	TL & OSL
Nebraska Sand Hills	57,000	20[M23]	OSL

Table ED2. Dune-field ages and areas. This is the data from Figure 2e tabulated and referenced. Dune fields with asterisks after their names are used in the geometric study. Dating technique codes in the right-most column are as follows: RAP, Repeat Aerial Photography OSL, Optically Stimulated Luminescence; IRSL, Infrared Stimulated Luminescence; ESR, Electron Spin Resonance; TL, Thermoluminescence; Nuclides, Cosmogenic Nuclide; MR, Magnetic Remanence; SI, Stratigraphically Interpreted.

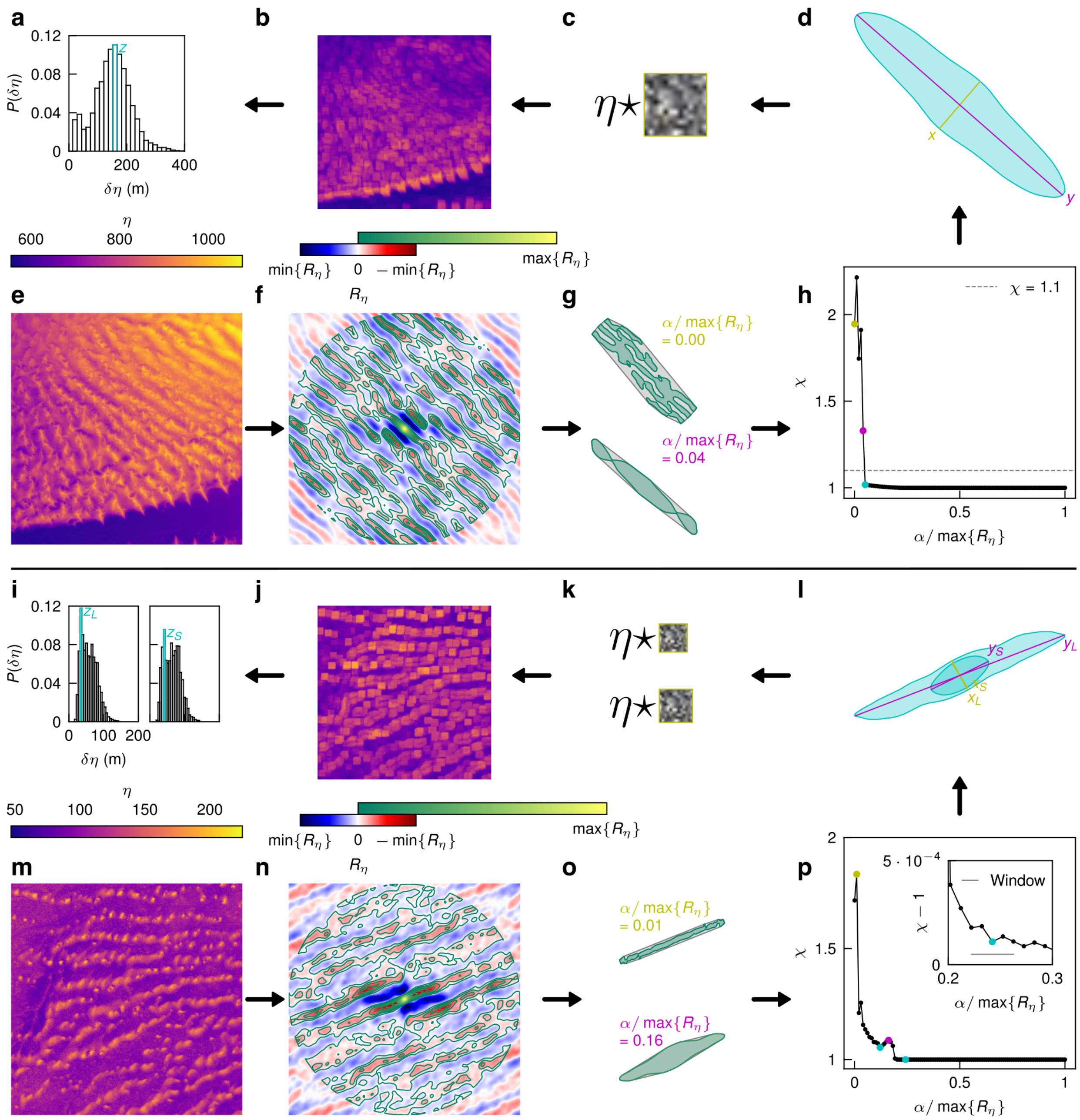

Figure ED1. Dune geometry extraction examples. Panels (**a–h**) and (**i–p**) are two examples of the algorithmic workflow (following the black arrows) to find dune geometry, note panels are at different scales. (**e** & **m**) ASTER topography η from the Namib Sand Sea (as in Fig. 1b) and Rub Al Khali. (**f** & **n**) Autocorrelation R_η of the topography (shown in blue-red with bottom colorbar) and contours, drawn within a circle to avoid orientation bias, for $0 \leq \alpha < \max\{R_\eta\}$ are highlighted (shown in green-yellow with top colorbar). (**g** & **o**) Example level-sets of α contours which inscribe the origin of R_η surrounded by their convex hulls. (**h** & **p**) The ratio of the level-set's convex hull's area to the level-set's area χ for increasing α, with the two examples from (g & o) marked in the text colors (yellow and magenta). In cyan are the level-sets that mark the dune geometries: in (h) this is the level-set of lowest α where $\chi < 1.1$ since $\chi(\alpha)$ monotonically decays, and in (p) it is the two largest α that are local minima in the $\chi(\alpha)$ plot (using a window of two neighbours as shown in the inset of the smaller dune). (**d** & **l**) The extracted level-sets representing dunes and their short-axis x (yellow) and long-axis y (magenta) identified; subscripts large (L) and small (S) are given for (p) for the star and linear dunes. (**c** & **k**) The convolution of topography η with a min-max box that retrieves the local range in values over width x (yellow), for (k) there are two convolutions, one for each dune wavelength x_S & x_L. (**b** & **j**) The result of the convolution, $\delta\eta$. For (j) only the large case is shown. (**a** & **i**) The PDF of $\delta\eta$ with the peak marking z, for (i) the two histograms with identical axes are shown.

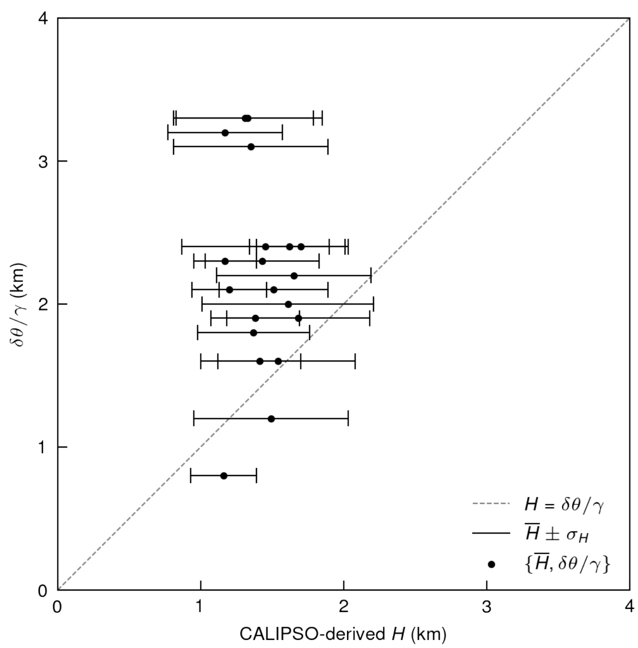

Figure ED2. **Mixed layer height measurement comparison.** CALIPSO-derived H values for 20 of 34 dunes measured by Andreotti *et al.*[10] against the proxy for mixed layer height $\delta\theta/\gamma$ reported in that study for each dune[10], where $\delta\theta$ is the seasonal range in surface potential temperature and γ is the lapse rate (note this is taken as a global constant $\gamma = 4$ K/km). CALIPSO-derived H values were taken within a 90-km radius from the dune for all available profiles in the period 2006-2016; total means (over 11 seasonal cycles) and standard deviations are shown. Omitted dunes are those within 90 km of the ocean or lack sufficient CALIPSO measurements to find a robust mean H. Analysis of this plot is given in Text S1.

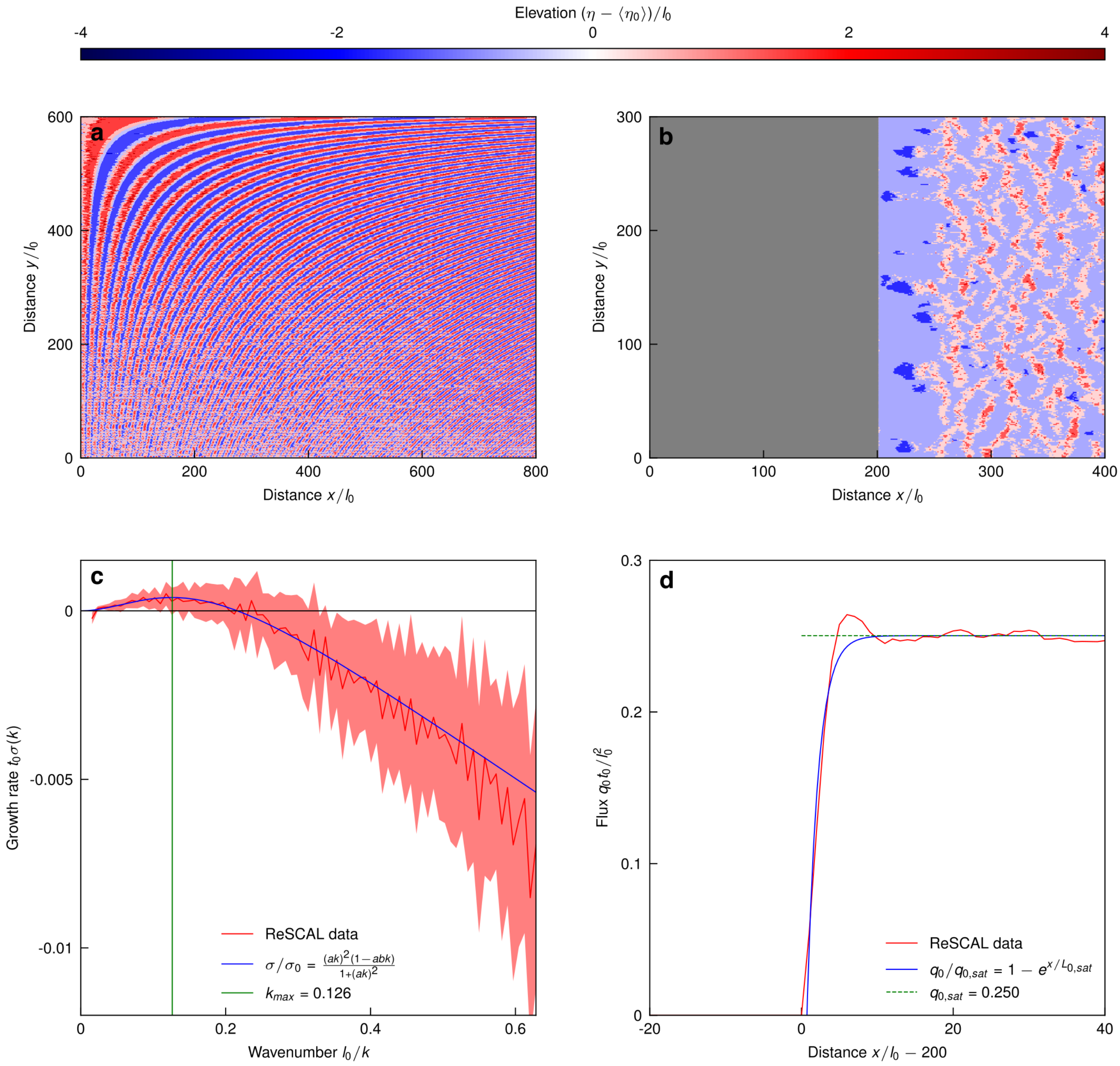

Figure ED3. ReSCAL scaling procedure. (**a**) Topography after $100t_0$ in an experiment where increasing small-amplitude topographic waves with span-wise y have been altered by flow. (**b**) Topography after $10t_0$ in an experiment where flow encounters a boundary from non-erodible bedrock (grey) to erodible sediment. The colorbar above applied to both (a) & (b). (**c**) The dispersion relation $\sigma(k)$ shown for the experiment in (a) (red line for mean, shading for standard deviation) with the fit (blue line) giving the maximally unstable wavelength (green line)[15]. (**d**) Span-wise mean of flux measured from tracers in the experiment shown in (b) (red line) and the fit (blue line) giving the saturated flux for $\tau_1 = 0\tau_0$ (green line)[M29].

Supplementary Information

Text S1 Mixed layer height resonance analysis

We see from explicit measurement of the dune wavelength x and mixed layer heights H (Fig. 3b) that the previously posited[10] identity $x = H$ does not prevail. This is at odds with the correlation of x and H using an implicit measurement of $H \approx \Delta\theta/\Gamma$, the ratio of the seasonal range in surface potential temperature $\Delta\theta$ (K) and the dry adiabatic lapse rate Γ (K/m)[10]. Here we suggest a few reasons for this inconsistency.

In principle certain obstacles on the planetary surface can emit internal gravity waves in the atmosphere even if the lowermost air layer of height h is neutrally stratified. In order for that to be the case, the horizontal wavenumber k of the obstacle has to be comparable with $1/h$. This is analogous to the 'tunnel effect' in quantum mechanics. In the case of very strong convection the wind profile is nearly uniform within the ABL and the wind shear is confined to the surface adjacent boundary layer of the depth that scales with the Obukhov length $L = -u_*^3\theta_0/(\kappa g\overline{w\theta})$ (m), where u_* (m/s) is the friction velocity, θ_0 (K) is the potential temperature at the surface, κ is Von Karman's constant, g (m/s^2) is gravity, and $\overline{w\theta}$ (mK/s) is the vertical turbulent flux of potential temperature[S1]. For internal gravity waves the intrinsic frequency must be less than the Brunt-Väisälä frequency $N = \sqrt{g/\theta\partial\theta/\partial z}$ (1/s), virtually leading to the inequality $kU < N$. Putting some numbers on this we have $N \approx 10^{-3}$ (1/s) and $k = 2\pi/2000$ (1/m) (where x is 2 km), resulting in $U \lesssim 1/\pi$ (m/s), well below that required to move sand. Indeed, a study of the boundary layer structure over the Nebraska Sand Hills found that there is no influence of the 2-km wavelength dunes on the MLH or crest-normal velocity perturbations in the presence of convection or large wind speeds[S2].

One could also argue that the lack of correlation does not necessarily imply that $x = H$ is not the end-state since dunes could still be coarsening and are at various stages of growth. However this argument implies that $x < H$, and we see clearly in Figure 3b that most dune fields have $x > H$. A similarly simple argument against the $x = H$ identity is that in real dune fields, dune wavelength is not sufficiently spatially correlated to maintain long-range resonance with an emitted wave. There is sufficiently high-frequency spatial variability in sand supply to exert control over dune size[28] and form[4] to stop long-range order in dune wavelength.

Comparing the measurements of the mixed layer height H, we see that the annual means measured with CALIPSO are such that $1 < H < 2$ km, whereas the annual means inferred from seasonal surface temperature ranges taken from Andreotti *et al.*[10] have a far larger range (Fig. ED2). We believe that the majority of the larger H spread in the latter comes from the poor estimate of the lapse rate Γ (K/m) as a global constant. It is well known that the lapse rate has significant spatiotemporal variation across Earth, e.g. seasonally and inversely with latitude[S3]. For example, the implicit value of $H = 3.5$ km in Vostok, Antarctica[10] is around an order of magnitude larger than convective values observed at a similar Antarctic weather measurement site (Concordia Dome C)[S4]. The Antarctic case is also an example of the challenge one faces finding *in situ* measurements of atmospheric properties in inherently isolated dune fields; the Vostok temperature timeseries is observed around 430 km from the dunes–likely too far to argue that wavelength x is resonant. Finally, we note that neither the CALIPSO nor the dune geometry measurements indicate a robust trend in increasing wavelength away from the coast, an effect observed in Andreotti *et al.*[10] potentially due to limited dune geometry data and bias in implicit H due to high ocean heat capacity.

Table S1. Mixed layer heights over dune fields. Processed CALIPSO data giving the MLH values and the observation time (local standard time) over each dune field in the dataset. The table is a concatenated list of each dune-field's list of measurements, where each dune-field's list begins with its name, the radius of the circular region of interest (ROI) around the center of the dune field (Table ED2), and the total number of observations. Details of the processing is given in Methods M4. This table is provided as an auxiliary file with the manuscript named '`TableS1.csv`'.

Table S2. Dune geometry measurements. Processed data on dune geometry and ERA-5 derived sand flux. Each tile is a unique row. The dune field the tile belongs to is given in the first column and the tile centroid coordinates in the second and third columns. Each tile is given a 'Large' and 'Small' dune type, wavelength (m), width (m) and height (m) values (which, if there is only one dune present in the tile, are duplicates). Dune types are abreviated: 'b', Barchanoid; 't', Transverse; 'l', Linear; 's', Star. The decadal mean resultant sand flux (m^2/yr) and decadal mean flux magnitude (m^2/yr) for each tile is also given; flux directionality is the former over the latter. Details of the processing is given in Methods M3 & Figure ED1. This table is provided as an auxiliary file with the manuscript named '`TableS2.csv`'.

Movie S1. ReSCAL numerical experiment timelapses. Shown are the 6 experiments of varying sand supply (rows: low, top; high, bottom.) and sand flux direction number F_N (columns: 1, left; 2, center; 5, right). Experiments are shown to the same scale ($F_N = 1$ experiments are $\sqrt{2}$ wider). To ensure form can be seen during coarsening, the colorbar is unique for each experiment at each timestep: the minimum and maximum elevations η (i.e. the colorbar limits) are written in the bottom corners of each frame to the nearest meter. In the top right, the timestep is written to the nearest 1 decimal place in years. White space within the frame is non-erodible bedrock. Note the dislocation creep in $F_N = 2$ experiments.

References

[S1] Hess, G. D. & Spillane, K. T. Estimation of the parameters of convection dynamics. *J. Aircr.* **25**, 862–864 (1988).

[S2] Mengesha, Y. G., Taylor, P. A. & Lenschow, D. H. Boundary-layer turbulence over the nebraska sandhills. *Boundary-layer meteorology* **100**, 3–46 (2001).

[S3] Stone, P. H. & Carlson, J. H. Atmospheric lapse rate regimes and their parameterization. *J. Atmospheric Sci.* **36**, 415–423 (1979).

[S4] Casasanta, G., Pietroni, I., Petenko, I. & Argentini, S. Observed and modelled convective mixing-layer height at dome c, antarctica. *Boundary-Layer Meteorol.* **151**, 597–608 (2014).